THE JOURNAL OF PHYSICAL CHEMISTRY C
A JOURNAL OF THE AMERICAN CHEMICAL SOCIETY

Cationic Ordering, Solid Solution Domain, and Diffuse Reflectance in Fe_2WO_6 Polymorphs

Stéphane Caubergh, Nami Matsubara, Françoise Damay, François Fauth, Dmitry D. Khalyavin
, Pascal Manuel, Abdelfattah Mahmoud, Dirk Poelman, Christine Martin, and
Bénédicte Vertruyen*

Cite this: *J. Phys. Chem. C* 2021, 125, 46, 25907–
25916

https://doi.org/10.1021/acs.jpcc.1c08314

Cationic Ordering, Solid Solution Domain and Diffuse Reflectance in Fe_2WO_6 Polymorphs

*Stéphane Caubergh[1], Nami Matsubara[2,3], Françoise Damay[3], François Fauth[4], Dmitry D. Khalyavin[5], Pascal Manuel[5], Abdelfattah Mahmoud[1], Dirk Poelman[6], Christine Martin[2], and Bénédicte Vertruyen[1,]**

[1] GREENMAT, CESAM Research Unit, Université de Liège, 4000 Liege, Belgium.

[2] CRISMAT, Normandie Univ., ENSICAEN, UNICAEN, CNRS, 14000 Caen, France.

[3] Université Paris-Saclay, CEA-CNRS UMR12, Laboratoire Léon Brillouin, 91191 Gif-sur-Yvette Cedex, France.

[4] ALBA-CELLS Synchrotron, BP1413, 08290 Cerdanyola del Vallès, Barcelona, Spain.

[5] ISIS Pulsed Neutron Facility, STFC Rutherford Appleton Laboratory, Chilton, Didcot, Oxfordshire OX11 0QX, United Kingdom.

[6] Department of Solid State Sciences, Lumilab, Ghent University, 9000 Ghent, Belgium

*email: b.vertruyen@uliege.be

ABSTRACT

Single phases of the α, β and γ polymorphs of the Fe_2WO_6 iron tungsten oxide were obtained through an aqueous solution route based on the combustion and heat treatment of a spray-dried precursor powder. Syntheses with Fe/W ratios $\neq 2$ identified a domain of solid solution consistent with a $Fe_{2-2x}W_{1+x}\square_xO_6$ scenario (x up to ~0.025) for the defect chemistry in the temperature range around 850°C. The crystallographic characterizations revealed a random cationic distribution in an α-PbO_2-type cell for the low temperature polymorph (α) and pointed to a reconstructive mechanism for the formation of polymorph β. A comparison of diffuse reflectance spectra confirmed the visual observation of minor colour differences between the polymorphs by revealing small shifts of the absorption threshold; the Kubelka-Munk function and Tauc plots were used for comparison of the polymorphs and confrontation of the results with relevant literature.

1. Introduction

Historically, the interest in the properties of Fe_2WO_6 was mostly focused on the magnetism and/or transport properties of its polymorphs, considered in the framework of the AB_2O_6 structures combining a magnetic cation B with an A cation of high formal charge.[1-9] In recent years, the environmentally benign character of iron has spurred the interest for iron-based oxides. Accordingly, Fe_2WO_6 has become the focus of much more varied investigations regarding the photo-electrochemical activity,[10-15] photocatalytic properties,[16-18] reversible capacity as a lithium ion battery electrode,[19-20] pseudocapacitance in electrochemical capacitors,[21] magneto-dielectric properties,[22] thermoelectric properties[23-24] and biological activity[25]. Indeed, half of the ~30 papers about Fe_2WO_6 have been published since 2014, with 9 of them published since 2020.

In view of this renewed interest, it is worthwhile to investigate several pending questions regarding Fe_2WO_6. Some of them concern the polymorphism of Fe_2WO_6. Most of the older literature and all of the recent papers focus on one polymorph only, usually either the high temperature γ polymorph[3-6,16,22-24] or the α polymorph obtained by low temperature solution routes[14,15,20,21,25]. In the early nineties Walczak et al.[7] identified a third polymorph, labelled β, whose synthesis required long heat treatments; shortly afterwards, Guskos et al.[8,9] reported some magnetic and electric transport data for the three polymorphs. To date, their work remains the only comparative study of the α/β/γ polymorphs and further work is needed to clarify the influence of the synthesis conditions on the polymorphism and on structural properties such as the cationic order/disorder. The comparison of characteristics such as the optical absorption has also become of interest in the context of the photo-electrochemical and photocatalytic applications for which Fe_2WO_6 has been recently considered.[10-18]

Solution routes are the best choice to prepare single phases of the three polymorphs by the same synthesis technique, since the reproducible synthesis of the low-temperature α polymorph by solid state reaction is difficult. Several solution-based syntheses of mixed iron-tungsten oxides were reported in literature in recent years, such as spray-pyrolysis for the synthesis of thin films[14,15] or various (co)precipitation procedures[17-21,25]. In the present work, a new procedure was developed, based on spray-drying an aqueous solution, followed by combustion and heat treatment of the spray-dried precursor. The spray-drying technique is an industrially up-scalable method suitable for the reproducible production of large quantities.[26,27] The composition of the solution was optimized so that all counter-ions decompose during the heat treatment and citric acid was used as a complexing agent to promote a homogeneous distribution of cations in the precursor powder. The synthesis procedure also allowed to prepare samples with well-controlled non-stoichiometric Fe/W ratios to investigate another unsettled issue in the Fe_2WO_6 literature, i.e. the existence of a solid solution domain.[6,10,23]

In the following, we first report about the crystallographic structures at room temperature for the three polymorphs, with particular emphasis on polymorph α for which synchrotron X-ray powder diffraction and neutron powder diffraction data were obtained for the first time. Results about the solid solution range for Fe/W ratios $\neq 2$ are then used to discuss the defect distribution in Fe_2WO_6 in the temperature range around 850°C, while data collected during the synthesis of the single phase samples provide information about the $\alpha \rightarrow \gamma$ and $\gamma \leftrightarrow \beta$ transitions. The next section presents the diffuse reflectance spectra collected on the single-phase samples of the different polymorphs, including the transformation into Tauc plots for a comparison with literature.

2. Methods

2.1. Materials.

Iron(III) nitrate $Fe(NO_3)_3.xH_2O$ (99%, Alfa-Aesar), iron (III) oxide Fe_2O_3 (99.9%, Alfa-Aesar), ammonium metatungstate $(NH_4)_6W_{12}O_{39}.xH_2O$ (AMT, 99.9%, Alfa-Aesar), tungsten oxide WO_3 (99.8%, Alfa-Aesar), citric acid monohydrate (>99%, Sigma-Aldrich), oxalic acid dihydrate (>99%, Sigma-Aldrich), HNO_3 (65 wt% in water, for analysis, Acros Organics), HCl (37 wt% in water, Acros, for analysis), NH_4OH (35 wt% in water, ExtraPure, Fisher), milliQ water.

2.2. Synthetic procedures.

2.2.1. Spray-drying synthesis using a citrate-based aqueous solution.

In a typical synthesis, the solution to be spray-dried was prepared by dissolving ammonium metatungstate powder into an acidified aqueous solution of iron(III) nitrate ($[Fe(NO_3)_3] \sim 1$ mol/l ; $[HNO_3] \sim 0.15$ mol/l). The exact concentration of iron in the stock solution and the water content in AMT were previously determined (see below). Citric acid was then added in 1:1 molar ratio with Fe and the pH was increased to 6.5 using concentrated ammonia. The transparent brown solution was diluted with milliQ water to reach a total concentration in cations of about 0.2 mol/l. The solution was spray-dried using a GEA Niro Mobile Minor spray-dryer with a rotary nozzle, a feed rate of 10 ml/min and inlet and outlet temperatures of 180°C and 130°C, respectively. The as-sprayed powder was placed as a 5 mm-thick layer in a broad Pyrex dish on a heating plate until auto-combustion was completed. For safety reasons, the combustion should be carried out away from flammable materials and preliminary tests on small amounts are recommended to check that the heat and gas releases are adequately handled. The resulting powder was then heated for 6 hours at 300°C in air. Further heat treatments at temperatures between 800°C and 950°C were performed to obtain the different polymorphs, as described in the 'Results and discussion' section.

2.2.2. Solid state synthesis of comparative samples.

Powders of α-Fe_2O_3 and WO_3 were weighed in a Fe/W = 2 ratio and mixed in an agate mortar. The powder mixture was then pressed with a uniaxial press in the shape of bars (2 x 2 x 12 mm^3). Different heat treatments were used to prepare the β and γ polymorphs (see text and/or figure captions).

2.3. Characterization techniques and procedures.

2.3.1. Chemical composition and microstructure. The metal content of the iron and tungsten salts was determined by thermogravimetry with a Setaram Labsys Evo instrument or by ICP-OES using an Agilent spectrometer. The Fe/W stoichiometry at different stages of the synthesis process and heat treatments was determined by ICP-OES after dissolution of Fe_2WO_6 in fuming hydrochloric acid overnight at 60 °C. Standard solutions of iron and tungsten were prepared by dilution of the respective standard solutions (Merck, traceable to SRM from NIST). The calibration curves were in the 10 – 100 mg/l range. Yttrium was added in all aliquots as the internal standard (10 mg/L) to account for the drift caused by temperature fluctuations in the plasma and yield fluctuations in the nebulizer of the ICP-OES instrument. Oxalic acid dihydrate $H_2C_2O_4.2H_2O$ was added in all aliquots containing tungsten species, in order to stabilize these species in solution. Scanning electron micrographs (SEM) were collected in secondary electron mode with a FEI XL30 ESEM coupled to an energy-dispersive analysis system. The powder samples were dispersed on carbon tape and coated with a gold layer. The BET specific surface area was determined from N_2 sorption isotherms measured at 77 K for relative pressure P/P^0 between 0 and 0.3 with a

Micromeritics Asap 2020 Plus instrument. Degassing was applied for 180 min at 150°C with a heating ramp of 10°C/min. The Rouquerol criteria were used to select the pressure range used to estimate the BET surface.[28]

2.3.2. Crystallographic structure.

Laboratory room temperature X-ray powder diffraction (XRD) characterizations were carried out in reflection geometry using Panalytical X-Pert and Bruker D8 Twin-Twin diffractometers with Cu-Kα radiation. Crystallite sizes were estimated with the TOPAS software using the fundamental parameters approach to model the instrumental contribution. Synchrotron X-ray powder diffraction (SXRPD) experiments were performed in transmission geometry on the BL04-MSPD beamline of the ALBA synchrotron.[29] Data were collected at 295 K using a high intensity mode detection setup (position sensitive detector MYTHEN), at wavelength $\lambda = 0.4427$ Å, with the sample enclosed in a spinning glass capillary (0.3 mm inner diameter). High-resolution neutron powder diffraction (HRNPD) data were collected at 295 K on the WISH time-of-flight (TOF) diffractometer at the ISIS neutron source.[30] The sample was loaded into a 6 mm diameter cylindrical vanadium can and mounted in a cryostat. Refinements of the crystal structures were performed using the FullProf Suite.[31] The background was described by a linear interpolation between selected background points (SXRPD data) or by a cubic spline interpolation (HRNPD data). In the case of the HRNPD data, banks 2–9 were included in the Rietveld calculations and a convolution pseudo-Voigt with back-to-back exponential functions was employed to model the peak shapes. The scattering angles for the different detector banks were as follows: banks 2/9, 58°; banks 3/8, 90°; banks 4/7, 122° and banks 5/6, 153°.

2.3.3. Diffuse reflectance spectroscopy.

Diffuse reflection spectroscopy measurements were carried out in the 300–2000 nm region with a Perkin Elmer Lambda 1050 UV/VIS/NIR spectrophotometer, equipped with a 150 mm spectralon coated integrating sphere with integrated InGaAs and PMT (photomultiplier) detectors. Absolute values of the diffuse reflectance were obtained following a calibration with a spectralon standard. The powder samples were packed in a powder cup with a quartz window.

3. Results and discussion

3.1. Development of the spray-drying synthesis route

Complexation was achieved by the addition of citric acid and basification of the mixed Fe-W aqueous solution, according to the procedure described in the Experimental section. Spray-drying of this solution yielded spherical particles with diameters in the 10 µm range (see SEM micrograph in Fig. 1a). When placed on a hot plate, the as-sprayed powder displayed a slow autocombustion driven by the mixture of nitrates (oxidizing agents) and citrates (reducing agents).[32] The mass loss of about 60 wt% during autocombustion created porosity (see SEM micrograph in Fig. 1b) and corresponds to an almost complete decomposition of the organic fraction, since the mass loss during a further heat treatment at 300°C in air for 6 hours did not exceed 2 wt%. Heat treatment at higher temperatures allowed to prepare single phases of the 3 polymorphs, as shown in Figure 1c and discussed in the next section.

During the investigation of the formation of the different polymorphs, the powders prepared by spray-drying were found to be more sensitive to tungsten loss by vaporisation at high temperatures than powders prepared by solid state reaction of Fe_2O_3 and WO_3. While the stoichiometry of the single phase samples shown in Fig. 1c was still in agreement with the nominal one, more extended heat treatments at 900°C or above resulted in a shift towards higher Fe/W ratios measured by ICP and increasing intensity of the Fe_2O_3 main peak in X-ray diffraction patterns (see Fig. S1 in Supplementary Information). Experiments comparing the surface and bulk of pellets confirmed that this effect is likely due to the higher specific surface area of the powders prepared by the spray-drying route (between 2 and 5 m^2/g vs. below 1 m^2/g for samples prepared by solid state reaction of the binary oxides oxides – see Figure S2 for SEM micrographs).

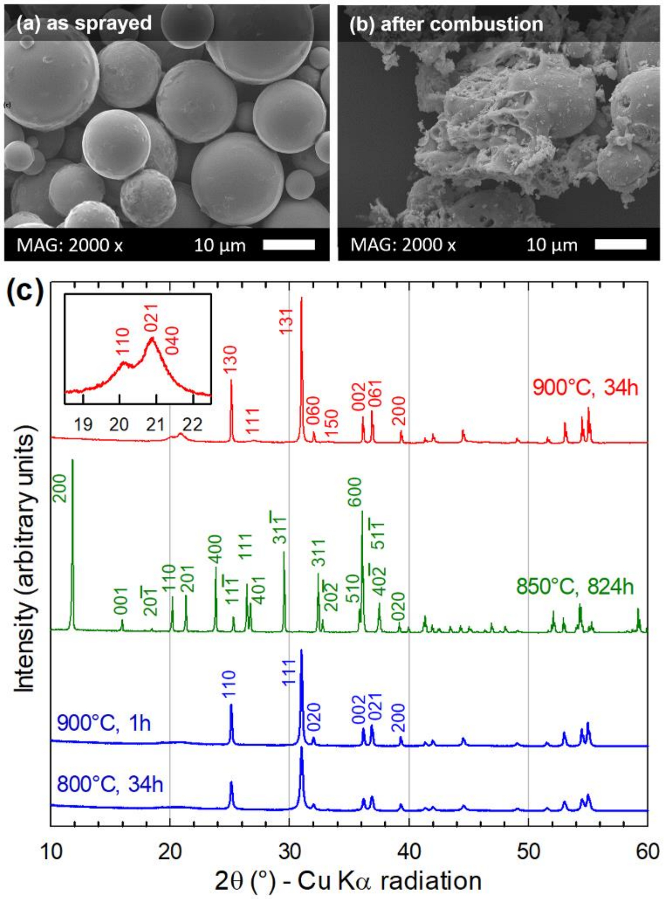

Figure 1. (a,b) Scanning electron micrographs of a typical as-sprayed powder and the same powder after combustion; (c) Laboratory X-ray diffractograms of the α (in blue), β (in green) and γ (in red) polymorphs obtained by heat treatment of a precursor powder with Fe/W = 1.96±0.04 at the temperature and for the duration indicated on each curve. The hkl indices correspond to crystallographic cells in the P*bcn*, P2$_1$/*a* and P*bcn* space groups for the α, β and γ polymorphs, respectively.

3.2. Crystallographic structures at room temperature

3.2.1. Polymorph α.

Earlier studies such as the work by Walczak et al.[7] reported polymorph α in samples prepared at temperatures around 800°C, with the presence of residual amounts of the binary oxides Fe_2O_3 and WO_3 which we also observed in the case of standard solid state reaction (not shown); further heat treatments of such samples to suppress the residual phases were found to initiate the transformation into the other polymorphic forms, as also reported by other authors.[7,10] Here the spray-drying route allowed us to obtain polymorph α as a single phase, judging from laboratory X-ray diffraction. The diffractograms in Fig. 1c show samples of polymorph α obtained after 34h at 800°C or after a shorter heat treatment at higher temperature (1h at 900°C) followed by quenching to room temperature. The two diffractograms differ only in the sharpness of the diffraction peaks, corresponding respectively to apparent crystallite sizes of 32 nm and 60 nm.

The structure of polymorph α is often reported as "columbite" in the literature, following the 1962 paper by Bayer[1], but it should be stressed that the superstructure peaks of the ordered A_2BO_6 columbite are absent. Indeed, the unindexed superstructure peaks observed by Bayer[1] for $ZnTa_2O_6$ and Fe_2WO_6 (with high and weak intensities, respectively) actually correspond to the superstructure peaks of the tri-α-PbO_2 structure identified at a later date for the γ polymorph of Fe_2WO_6 [3] and $ZnTa_2O_6$ [33] – These superstructure peaks were not included in the comparative table of Walczak et al.[7]. As recently proposed by Espinosa-Angeles et al.,[21] the structure of polymorph α should therefore rather be reported as α-PbO_2-type to reflect the random cationic distribution. This absence of superstructure peaks is confirmed when reviewing the diffraction data obtained by other authors for samples prepared at 800°C (either powders[2] or films[14,15]). The good homogeneity of the cationic distribution in the spray-dried or other solution-based precursors favours the formation of polymorph α following diffusion over very short distances, by comparison with the longer distances required in the case of solid state reaction between the binary oxides.

The room temperature crystallographic structure of the sample of polymorph α obtained after 34 hours at 800°C was studied by a combination of synchrotron X-ray powder diffraction (SXRPD) and high-resolution neutron powder diffraction (HRNPD). The Rietveld refinement in the P*bcn* space group, including a minor contribution (below 0.5 %) from hematite (H peaks), is shown in Figure 2 together with the cell parameters and crystallographic parameters; a crystallographic information file is provided as supplementary information. A Rietveld refinement based on laboratory X-ray data, very recently reported for a sample prepared by a polyol solution route, is in good agreement with this structural model.[21] However, the excellent signal-to-noise ratio offered by our synchrotron data reveals that a few very small peaks remain unindexed at d = 5.60 Å, 4.59 Å and 3.28 Å. None of these peaks matches a columbite superstructure. The first two occur at positions corresponding to the 010 and 100 reflections of the orthorhombic cell, extinct in the P*bcn* space group. The third one is very close to the position of the main reflection of V_2WO_6 trirutile,[34] suggesting the hypothesis of a metastable Fe_2WO_6 trirutile phase. In summary, the evidence available so far points to an α-PbO_2-type structure with possible minor local deviations.

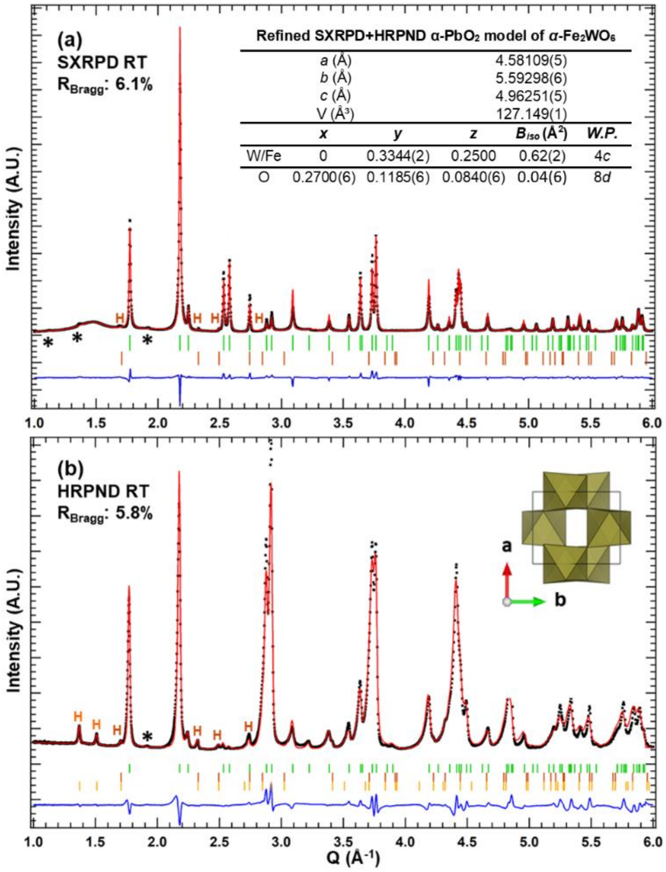

Refined SXRPD+HRPND α-PbO_2 model of α-Fe_2WO_6

	a (Å)		4.58109(5)		
	b (Å)		5.59298(6)		
	c (Å)		4.96251(5)		
	V ($Å^3$)		127.149(1)		
	x	***y***	***z***	B_{iso} ($Å^2$)	***W.P.***
W/Fe	0	0.3344(2)	0.2500	0.62(2)	4*c*
O	0.2700(6)	0.1185(6)	0.0840(6)	0.04(6)	8*d*

Figure 2. Room temperature SXRPD and HRNPD data as a function of Q = 2π/d for α-Fe_2WO_6 (Fe/W = 1.96±0.04, prepared by the citrate spray-drying route and heat treatment at 800°C for 34 hours) and combined Rietveld refinement in the α-PbO_2-type *Pbcn* unit cell shown in inset. Black dots = experimental data; red continuous line = calculated curve; vertical marks = Bragg reflections for α-Fe_2WO_6 (in green) and hematite (dark and light orange for nuclear and magnetic reflections, respectively); blue continuous line = difference between the experimental and calculated profiles, showing the imperfect modelling of the peak shapes (background-corrected R_{wp} = 15 % for SXRPD, 17 % for HRNPD); H = hematite reflections; stars = unindexed reflections.

3.2.2. Polymorph β.

The formation of polymorph β is known to progress very slowly,[7,35] and the samples prepared here by spray-drying were no exception with a total residence time at 850°C of several weeks to obtain a single phase. The room temperature crystallographic structure of this sample, determined from synchrotron and neutron diffraction, is in complete agreement with the structure that we recently solved for a sample prepared by solid state reaction of the binary oxides.[35] The Rietveld refinement plots and a table of the cell parameters and the crystallographic parameters are provided as supplementary information (Fig. S3 and Table S1).

3.2.3. Polymorph γ.

This polymorph was reported with a tri-α-PbO_2 structure type by Senegas and Galy in 1974 based on single crystal diffraction data.[3] The long-range ordering of the Fe/W cations in the zig-zag chains of octahedra (Fig. S4a) is different from the hypothetical ordered columbite structure (Fig. S4b) and leads to superstructure reflections which distinguish polymorph α from polymorph γ. Formed at the highest temperatures, polymorph γ has been the most studied polymorph in the literature so far and the structure proposed by Senegas and Galy[3] was confirmed for polycrystalline samples by several groups[7,22,23]. The samples prepared here by the spray-drying route display rather weak and ill-defined order peaks after 34 h at 900°C, as shown in the inset of Fig. 1c. The cationic ordering during the α→ γ transition is further discussed in a later section.

3.3. Composition range of solid solution

As mentioned in the captions of Figures 1 and 2, the diffractograms shown in the previous section correspond to samples with 1.96 Fe/W ratio. This composition was selected as the middle of the solid solution range identified during an earlier step of our work, where spray-dried precursors with Fe/W ratios ranging from 1.88 to 2.11 were submitted to heat treatments at 850°C in air. Figure 3a shows the laboratory X-ray diffractograms collected after 10 h at 850°C for the compositions just below and above the limits for the appearance of Fe_2O_3 or WO_3 reflections. Apparently single-phased products were obtained for Fe/W ratios between 1.91 ± 0.04 and 2.00 ± 0.04, where the error bar corresponds to ± 2 standard deviations of the ICP measurement. Extending the heat treatment to 130 h or 440 h (not shown) led to sharper reflections and a transition towards polymorph β but did not modify the limits of the solid solution range.

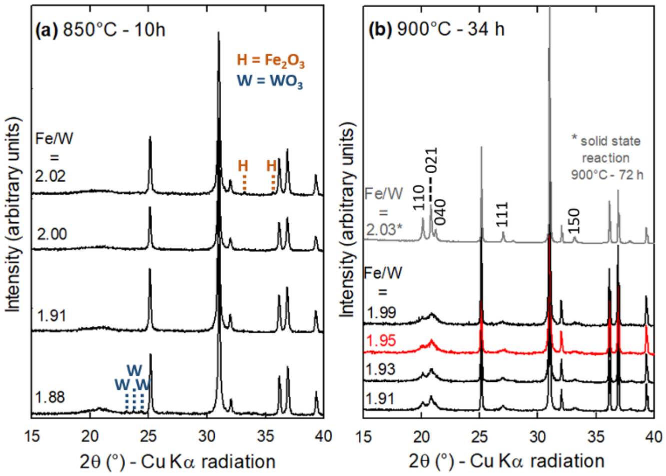

Figure 3. (a) Laboratory X-ray diffractograms collected after 10 h at 850°C for powders with different Fe/W ratios; the W and H symbols indicate the appearance of WO_3 and Fe_2O_3 reflections outside the solid solution range. (b) Laboratory X-ray diffractograms collected after 34 h at 900°C for powders with different Fe/W ratios within the solid solution range, compared to the diffractogram of a sample prepared by solid state reaction of the binary oxides. The hkl indices correspond to reflections characteristic of the γ polymorph in the tri-α-PbO_2 unit cell. The Fe/W values in the two figures were measured by ICP with an error bar of ±0.04, corresponding to ±2 standard deviations.

These results are consistent with a general formula $Fe_{2-2x}W_{1+x}\square_{x}O_6$, where the excess of tungsten in the Fe/W < 2 range is accommodated on positions normally occupied by Fe with a compensation of the effective charge by vacancies: $2\ Fe_{Fe} \rightarrow W_{Fe}^{\bullet\bullet\bullet} + V_{Fe}'''$ in Kröger-Vink notation. A similar compensation mechanism involving only the cationic sites would not be possible in the Fe/W > 2 range since substitutions of Fe on positions normally occupied by W would require vacancies on the oxygen sites: $2\ W_W + 3\ O_O \rightarrow 2\ Fe_W''' + 3\ V_O^{\bullet\bullet}$. The fact that the single-phase domain does not extend towards the Fe-rich compositions suggests that such vacancies in the oxygen network do not occur in the case of heat treatments at temperatures not exceeding 850°C.

The $Fe_{2-2x}W_{1+x}O_6$ scenario proposed here should also be confronted to relevant literature. Both Birchall et al.[6] and Leiva et al.[10] reported single-phase compounds only for Fe/W nominal compositions well below 2, and below the solid solution domain determined here. We believe that the actual compositions of their samples probably corresponded to higher Fe/W ratios than the nominal ones, since the heat treatments were conducted at 950°C or 1000°C for durations ranging from 92 hours up to 3 weeks. Indeed, Birchall et al.[6] reported a contribution of Fe_2O_3 in Mössbauer spectra increasing to 44% after 3 weeks of heat treatment, together with a loss of about 25 % of the total sample mass. This points to a loss of tungsten as a volatile oxide at high temperature. The diffusion of WO_3 in gaseous phase was reported by Thomas and Ropital in their study about the formation mechanisms of iron tungstates in different atmospheres.[36] As mentioned above, we also observed a loss of tungsten in the spray-dried samples heated for long durations at 900°C and above; this was the reason why most of the study of the solid solution range was carried out at 850°C.

Recently Schuler et al.[23] proposed the formula $Fe_{2-x}^{3+}Fe_x^{2+}WO_{6-x/2}$ for a sample of polymorph γ which was characterized by synchrotron XRD and by XPS, amongst other techniques. The authors found that a small contribution of Fe^{2+} species (3% of total Fe content) improved the fit of the XPS spectra and that the inclusion of 2% oxygen vacancies on one of the oxygen sites in the Rietveld refinement of the structural model improved the fit of the synchrotron data (although, as noted by the authors, there is a considerable uncertainty due to the low electronic density of oxygen). The possible presence of Fe^{2+} had already been proposed in an earlier work by Leiva et al.[37]. Both Schuler et al.[23] and Leiva et al.[37] used heat treatments at higher temperatures than the ones considered here. Independently of speculations about the actual cationic compositions, this difference in temperature could affect the equilibrium composition corresponding to $P(O_2)$ ~0.2 bar and influence other characteristics such as the cationic ordering discussed in the next section.

3.4. Cationic ordering in the $\alpha \rightarrow \gamma$ transition

The structural difference between the α and γ polymorphs results from the ordering of the Fe and W cations leading to a superstructure with a tripling of the unit cell (Fig. S4a). These additional peaks are indexed in Figure 3b, where the comparison between the diffractograms of samples prepared by spray-drying with a reference sample obtained by standard solid state reaction of Fe_2O_3 and WO_3 (dark gray pattern) reveals much sharper superstructure peaks for the solid state sample. The existence of Fe/W atomic disorder in polymorph γ was already recognized by Senegas and Galy who found some atomic disorder even in a single crystal.[3] In Table 1 we use values of apparent crystallite size as a parameter to quantify the broadening of the peaks. In the case of the samples of polymorph γ, the apparent crystallite size deduced from the superstructure reflections is much smaller than the values associated to the reflections common to both polymorph α and γ (i.e., the reflections arising from the small α-PbO_2 cell). For the sample prepared by spray-drying, we found almost no change of the superstructure peaks as a function of treatment time at 900°C (not shown). This suggests that the good homogeneity of the cationic distribution in the spray-dried precursor leading to the easy formation of the disordered polymorph α does not favour further evolution by cationic reordering into polymorph γ. This hypothesis is supported by the observation that, amongst the spray-dried samples in Figure 3b, the samples with the lower Fe/W ratios have slightly sharper superstructure peaks: as discussed in the previous section, a deviation towards Fe/W < 2 is believed to be associated to cationic vacancies, which would help cationic mobility.

Table 1. Comparison of peak broadening in X-ray diffractograms, parameterized as apparent crystallite size.

Polymorph α, SD, 800°C/34h	30 nm
Polymorph α, SD, 900°C/1h	60 nm
Polymorph γ, SD, 900°C/34h	110 nm – superstructure peaks 10 nm
Polymorph γ, SS, 900°C/48h + 950°C/24h	230 nm – superstructure peaks 50 nm
Polymorph β, SD, 850°C/824h	380 nm
Polymorph β, SS, 850°C/504h	430 nm

SD = spray-drying route, diffractograms shown in Figure 1 (and 3b for the γ sample); SS = standard solid state reaction, diffractogram of γ sample shown in Figure 3b

3.5. Formation of polymorph β and reversibility of the γ ↔ β transition

As already mentioned, the formation of the β polymorph required long heat treatments. The X-ray diffractograms collected after 440 h, 632 h and 824 h at 850°C, plotted in Figure 4, show that the β reflections are sharp even at the early stages. This suggests that the formation of polymorph β takes place through a reconstructive phase transition,[38] contrary to the disorder-order character of the α → γ transition. The SEM micrographs shown in Fig.4(e,f) reveal that the formation of the β polymorph is accompanied by the appearance of larger particles assembled into platelet shapes. Indeed, laboratory XRD data collected on packed powder display a tendency to preferential orientation, manifested as an enhanced intensity of the h00 reflections.

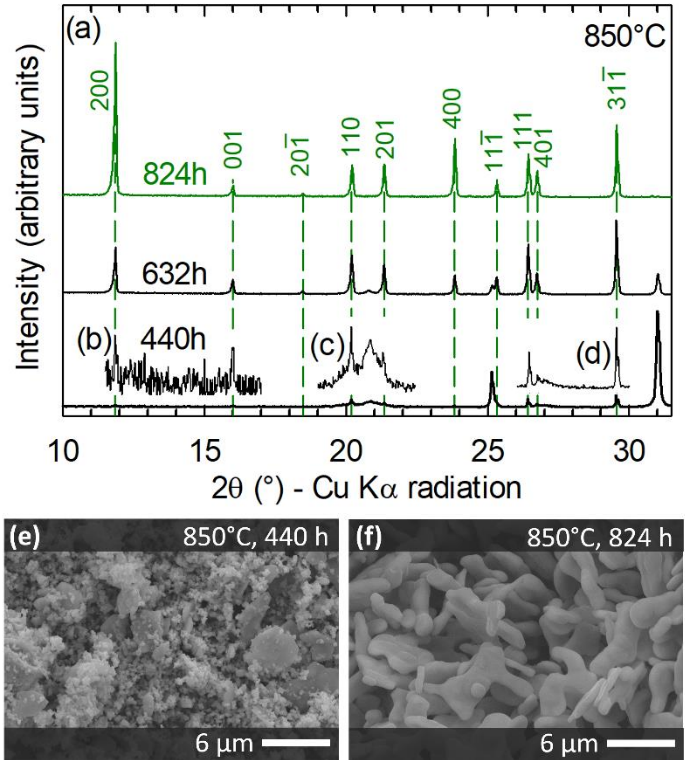

Figure 4. (a) Laboratory X-ray diffractograms collected after 440 h, 632 h or 824 h at 850°C for a powder with Fe/W = 1. 96±0.04 prepared by the citrate spray-drying route; the hkl indices and dashed vertical lines correspond to the reflections of the β polymorph. (b,c,d) Insets in figure (a) showing three 2θ-ranges of the 440 h diffractogram with magnified intensity scale. (e,f) Scanning electron micrographs of the powders after 440 h or 824 h at 850°C.

As already observed by Walczak et al.[7], the β polymorph can also form when starting from the γ polymorph. This was observed both when annealing at 850°C the sample of partially-ordered γ polymorph obtained by heat-treatment of the spray-dried precursor (Figure S5a) and when annealing at 900°C the reference γ polymorph prepared by solid state reaction (Figure S5b). Regarding the reversibility of the $\gamma \leftrightarrow \beta$ transition mentioned by Walczak et al.[7], we could replicate it only in the case of the solid state reaction samples; extended heat treatment at 950°C of the β polymorph prepared by the spray-drying route led to the appearance of hematite peaks (resulting from loss of tungsten) without any sign of a polymorphic transition. This suggests that the shift in stoichiometry towards tungsten-poor compositions might inhibit the $\beta \rightarrow \gamma$ transition.

3.6. Influence of polymorphism on the optical properties: diffuse reflectance spectroscopy

Visual inspection of the samples of single-phase polymorphs prepared by the spray-drying route or by solid state reaction (Figure 5a) reveals colours ranging from brown (for the two samples of α polymorph and the sample of poorly-ordered γ polymorph) to almost black (for the sample of γ polymorph prepared by solid state reaction), going through an intermediate dark purple-brown (for the two samples of β polymorph). Diffuse reflectance spectroscopy (DRS) measurements were carried out for all six samples. The curves of diffuse reflectance R_∞ vs. wavelength λ (Figure S6a) were transformed into plots of the Kubelka-Munk (KM) function $F(R_\infty)=(1-R_\infty)^2/(2R_\infty)$ (Figure S6b). The considerable popularity of this Kubelka-Munk transformation is due to the fact that it approximates the absorption curve if scattering effects can be considered as slowly varying within the investigated wavelength range.[39] Normalizing the KM curves as shown in Figure 5b allows us to compare the position of the main absorption threshold and confirms the trend observed by the visual inspection of colours. As in other absorption or KM spectra of oxides containing d^5 Fe^{3+}

cations (Fe_2O_3 [39-43], Fe_2TiO_5 [44]), the KM spectra of the Fe_2WO_6 polymorphs also display pre-threshold features resulting in more complex curves than those observed for oxides of d^0 cations such as TiO_2 or WO_3. At lower wavelengths, the well-ordered samples of Fe_2WO_6 (i.e., the two samples of polymorph β and the sample of polymorph γ prepared by solid state reaction) display a maximum at about 550 nm, while the maximum appears around 500 nm for the randomly- or poorly-ordered samples (i.e., the two samples of polymorph α and the sample of polymorph γ prepared by spray drying). Amongst the three Fe_2WO_6 polymorphs, the KM curve of polymorph β shows the closest similarity to hematite Fe_2O_3 [39] with a well-developed bump around 900 nm and a shoulder around 670 nm.

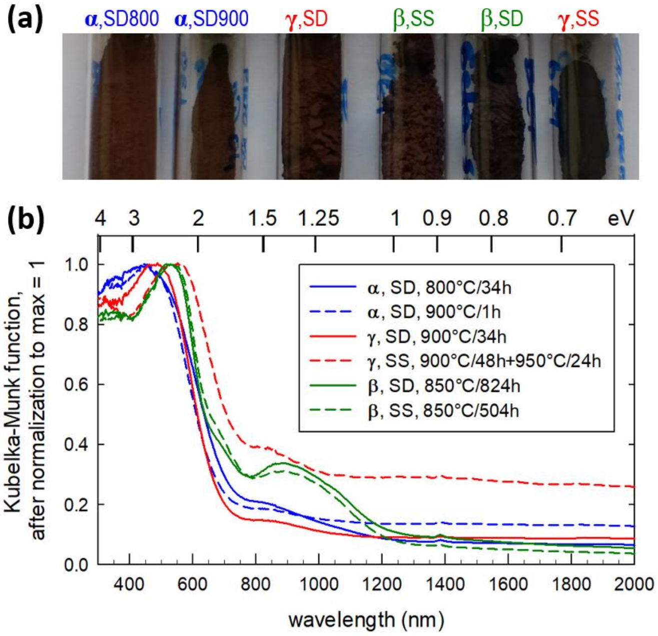

Figure 5. (a) Colour photographs and (b) normalized Kubelka-Munk function $F(R_\infty)=(1-R_\infty)^2/(2R_\infty)$ of the samples of single-phase polymorphs prepared by the spray-drying route (SD) or by solid state reaction (SS).

Going beyond these observations towards an assignment of the bands is the obvious next step. However, it turns out that even the interpretation of the absorption spectrum of hematite is still a matter of some debate.[45] The most detailed assignments for hematite remain those proposed several decades ago, based on ligand field theory and Tanabe-Sugano diagrams.[39-43] Most of these schemes agree in attributing the lower energy features to Fe d-d ligand field transitions, with ligand-metal charge-transfer transitions occurring at higher energies. For example, considering a cubic symmetry of the crystal field, the band assignment proposed by Sherman and Waite suggests that the bump at about 900 nm and the shoulder around 670 nm could be due to $^6A_1 \rightarrow {}^4T_1$ and $^6A_1 \rightarrow {}^4T_2$ transitions between $(t_{2g})^3(e_g)^2$ and $(t_{2g})^4(e_g)^1$ configurations, respectively.[39]

However, it was always recognized that these early assignments assumed that an analysis suitable for dilute Fe^{3+} cations in a host phase could be adapted to extended solids such as iron oxides.[39] The progress in computing capabilities now allows for more advanced treatments, either correlated wave-function methods such as embedded cluster schemes[46] or beyond-DFT methods such as many-body perturbation followed by Bethe–Salpeter calculations[47]. In the ongoing development of these computationally demanding methods, Fe_2O_3 is frequently chosen as a model compound.[47-49] Recent reports show promising improvements in the agreement that can be achieved between experimental and calculated absorption spectra.[47,50] Hopefully, further progress in the next years will allow these computational methods to become relevant tools for the interpretation of the experimental spectra. We expect that the dataset for the three Fe_2WO_6 polymorphs will then be a very interesting case study.

As a further step in the analysis of DRS data, the similarity between KM function and optical absorption is frequently used to estimate an experimental "optical band gap". The common procedure is based on equations derived from the Tauc relationship $\alpha h\nu = B\,(h\nu - E_{g,Tauc})^n$, where α

is the absorption coefficient, $n = 2$ for an indirect allowed transition and $n = 1/2$ for a direct allowed transition.[51] Initially developed for amorphous germanium semiconductors,[52] this formalism has been widely applied to a broad range of materials, including ternary oxides,[14,16,24,53-55] as a way to report absorption or diffuse reflectance data in plots of $[\alpha h\nu]^{1/n}$ or $[F(R_\infty)\ h\nu]^{1/n}$ vs $h\nu$, from which direct and/or indirect $E_{g,Tauc}$ gap values are extracted.[51]

Predictably, the complex shape of the KM spectra of the Fe_2WO_6 samples is transferred to the Tauc plots shown in Figure 6. As a result, the uncertainty on the $E_{g,Tauc}$ values discussed in the next paragraphs should be considered as significantly larger than the ±0.02 eV error bar associated to the fitting of a straight line to the linear range of the curves. In particular, the presence of the pre-threshold features means that these $E_{g,Tauc}$ values should probably be considered as a lower bound for the band gap energy.[56]

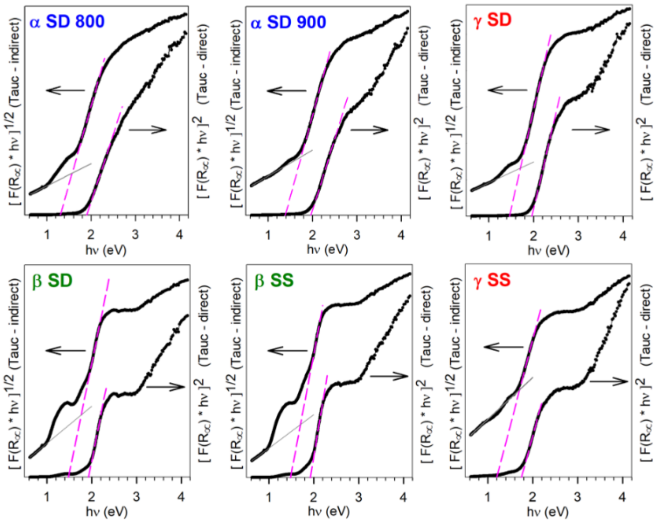

Figure 6. Transformation of the Kubelka-Munk $F(R_\infty)$ curves into Tauc plots $[F(R_\infty)\ h\nu]^{1/2}$ vs $h\nu$ (left-hand axes) and $[F(R_\infty)\ h\nu]^2$ vs $h\nu$ (right-hand axes). The pink dashed lines correspond to linear extrapolations to determine indirect and direct $E_{g,Tauc}$ values. The thin dark-grey lines correspond to sloped baselines extrapolated from the $h\nu < 0.8$ eV range.

Since the plots in Figure 6 do not allow for an obvious conclusion whether the equation for a direct or indirect band gap is most appropriate, we follow common usage and report both. The pre-threshold features are respectively suppressed and enhanced in the $[F(R_\infty)\ h\nu]^2$ vs hν and $[F(R_\infty)\ h\nu]^{1/2}$ vs hν plots. As a result, a direct $E_{g,Tauc}$ gap can be easily estimated from the intersection of the linear extrapolation with the abscissa axis, with values between 1.9 eV and 2.0 eV for all samples except the sample of polymorph γ prepared by solid state reaction which displays a value of about 1.75 eV. This is in rather good agreement with the values of 1.82 eV and 1.84 eV reported by Rawal et al.[16] and Schuler et al.[24], respectively, based on diffuse reflectance data collected on samples of polymorph γ. On the other hand, assuming an indirect $E_{g,Tauc}$ gap and extracting this from the $[F(R_\infty)\ h\nu]^{1/2}$ vs hν plots is less straightforward: the intersections of the linear extrapolation with the abscissa axis correspond to values between 1.2 eV and 1.45 eV but higher values are obtained if a sloped offset baseline in considered. For example, defining such a baseline as the linear extrapolation of the < 0.8 eV range of the plot results in values of about 1.7-1.75 eV for the indirect $E_{g,Tauc}$ gap of all samples except the sample prepared at the lowest temperature (1.55-1.6 eV for polymorph α prepared at 800°C). These values are similar to the 1.6-1.7 eV indirect bandgap reported by Abdi et al.[14] based on the Tauc plots of the absorption spectrum of Fe_2WO_6 thin films. Although Abdi et al. comment that the modest slope of the absorption coefficient plot suggests an indirect transition[14], they also reported direct gap values for the same films. These 2.3-2.45 eV values are close to the 2.3 eV gap obtained in a DFT (HSE03) calculation carried out by Schuler et al.[24], who also studied iron(II) tungstate ($FeWO_4$). In Fe_2WO_6, these authors found oxygen and iron orbitals to be the major contributors to the top of the valence band and the bottom of the conduction band, respectively. In this context it is also interesting to note that in Fe_2O_3 photo-anodes,[45] the onset of photocurrent usually occurs at higher energies than the absorption edge in the optical spectrum so that the transitions near the absorption edge are believed to create *localized* excited states.

4. Conclusions

The aqueous solution route is beneficial for the synthesis of polymorph α, whose crystallographic structure was refined with a random cationic distribution in an α-PbO_2-type cell. On the other hand, the homogeneity of the cationic distribution in the spray-dried precursor powder limits the degree of cationic ordering over long distances which can be achieved during the α → γ transition. The formation of a single phase of polymorph β requires several weeks of heat treatment. The sharpness of the diffraction peaks even at the earliest stages of the transition points to a reconstructive mechanism for the formation of polymorph β. Regarding the domain of solid solution at 850°C, the Fe/W ratios ranging between 1.91 and 2.00 are consistent with a $Fe_{2-2x}W_{1+x}\square_xO_6$ scenario. Polymorphism is associated with small shifts of the absorption threshold in the DRS spectra and with observed differences in the pre-threshold region.

ASSOCIATED CONTENT

Supporting Information.

The following files are available free of charge.

ICP measurements of Fe/W ratio after various heat treatments; Rietveld refinement, cell parameters and crystallographic parameters of polymorph β obtained by the spray-drying route; tri-α-PbO_2 structure of polymorph γ and hypothetical ordered columbite structure; Laboratory X-ray diffractograms showing the γ→β transition in spray-dried and solid-state samples; Diffuse reflectance spectra and corresponding Kubelka-Munk function of the samples of single-phase polymorphs prepared by the spray-drying route or by solid state reaction (pdf file).

Room temperature structure of the α polymorph (cif file)

AUTHOR INFORMATION

Corresponding Author

*E-mail for B. Vertruyen: b.vertruyen@uliege.be

Author Contributions

The manuscript was written through contributions of all authors. All authors have given approval to the final version of the manuscript.

Notes

The authors declare no competing financial interest.

ACKNOWLEDGMENT

S.C. thanks the « Fonds pour la Formation à la Recherche dans l'Industrie et dans l'Agriculture - FRIA » (Belgium) for a PhD fellowship (Grant number: 5200119F). S.C. and B.V. are grateful to the University of Liège and FRS-FNRS (Belgium) for travel and equipment grants. The authors thank Vincent Delaval for BET measurements.

REFERENCES

1. Bayer, G. Isomorphie- und Morphotropiebeziehungen bei Oxyden mit TiO_2-typ und Verwandten Strukturen. *Ber. Dtsch. Keram. Ges.* **1962**, *39*, 535-554.

2. Parant, C. ; Bernier, J.C. ; Michel, A. Sur Deux Formes Orthorhombiques de Fe_2WO_6. *C. R. Acad. Sc. Paris Serie C* **1973**, *276*, 495-497.

3. Senegas, J.; Galy, J. L'Oxyde Double Fe_2WO_6. I. Structure Cristalline et Filiation Structurale. *J. Solid State Chem.* **1974**, *10*, 5-11.

4. Weitzel, H. Magnetische Strukturen von $NiNb_2O_6$ und Fe_2WO_6. *Acta Crystallogr. Sect. A* **1976**, *32*, 592-597.

5. Pinto, H.; Melamud, M.; Shaked, H. Magnetic Structure of Fe_2WO_6, a Neutron Diffraction Study. *Acta Crystallogr. Sect. A* **1977**, *33*, 663-667.

6. Birchall, T.; Hallett, C.; Vaillancourt, A.; Ruebenbauer, K. A Study of Iron-Tungsten Oxides and Iron-Chromium-Tungsten Oxides. *Can. J. Chem.* **1988**, *66*, 698-702.

7. Walczak, J.; Rychiowska-Himmel, I.; Tabero, P. Iron(III) Tungstate and Its Modifications. *J. Mater. Sci.* **1992**, *27*, 3680-3684.

8. Guskos, N.; Sadlowski, L.; Typek, J.; Likodimos, V.; Gamari-Seale, H.; Bojanowski, B.; Wabia, M.; Walczak, J.; Rychlowska-Himmel, I. Magnetic and EPR Studies of α-, β-, and γ-Fe_2WO_6 Phases at Low Temperatures. *J. Solid State Chem.* **1995**, *120*, 216-222.

9. Guskos, N.; Likodimos, V.; Glenis, S.; Patapis, S.K.; Palilis, L.C.; Typek, J.; Wabia, M.; Rychlowska-Himmel, I. Electrical Transport and EPR Properties of the α, β, and γ Phases of Fe_2WO_6. *Phys. Rev. B* **1999**, *60*, 7687-7690.

10. Leiva, H.; Dwight, K.; Wold, A. Preparation and Characterization of Conducting Iron Tungstates. *J. Solid State Chem.* **1982**, *42*, 41-46.

11. Khader, M.M.; Saleh, M.M.; El-Naggar, E.M. Photoelectrochemical Characteristics of Ferric Tungstate. *J. Solid State Electrochem.* **1998**, *2*, 170-175.

12. Meyer, R.; Sliozberg, K.; Khare, C.; Schuhmann, W., Ludwig, A. High-Throughput Screening of Thin-Film Semiconductor Material Libraries II: Characterization of Fe-W-O Libraries. *ChemSusChem* **2015**, *8*, 1279-1285.

13. Kollender, J.P.; Mardare, A.I.; Hassel, A.W. Localized Photoelectrochemistry on a Tungsten Oxide–Iron Oxide Thin Film Material Library. *ACS Comb. Sci.* **2013**, *15*, 601-608.

14. Abdi, F.F.; Chemseddine, A.; Berglund, S.P.; van de Krol, R. Assessing the Suitability of Iron Tungstate (Fe_2WO_6) as a Photoelectrode Material for Water Oxidation. *J. Phys. Chem. C* **2017**, *121*, 153-160.

15. Lin, H.; Long, X.; An, Y.; Yang, S. In situ Growth of Fe_2WO_6 on WO_3 Nanosheets to Fabricate Heterojunction Arrays for Boosting Solar Water Splitting. *J. Chem. Phys.* **2020**, *152*, 214704.

16. Rawal, S.B.; Ojha, D.P.; Sung, S.D.; Lee, W.I. Fe_2WO_6/TiO_2, an Efficient Visible-Light Photocatalyst Driven by Hole-Transport Mechanism. *Catal. Commun.*, **2014**, *56*, 55-59.

17. Wang, Y.; Zeng, Y.; Chen, X.; Wang, Q.; Wan, S.; Wang, D.; Cai, W.; Song, F.; Zhang, S.; Zhong, Q. Tailoring Shape and Phase Formation: Rational Synthesis of Single-Phase $BiFeWO_x$ Nanooctahedra and Phase Separated Bi_2WO_6-Fe_2WO_6 Microflower Heterojunctions and Visible Light Photocatalytic Performances. *Chem. Eng. J.* **2018**, *351*, 295-303.

18. Xin, Y.; Zhang, N.; Li, Q.; Zhang, Z.; Cao, X.; Zheng, L.; Zeng, Y.; Anderson, J.A. Selective Catalytic Reduction of NO_x with NH_3 over Short-Range Ordered W-O-Fe Structures with High Thermal Stability. *Appl. Catal. B* **2018**, *229*, 81-87.

19. Kendrick, E.; Swiatek, A.; Barker, J. Synthesis and Characterisation of Iron Tungstate Anode Materials. *J. Power Sources* **2009**, *189*, 611-615.

20. Xu, K.; Shen, X.; Ji, Z.; Yuan, A.; Kong, L.; Zhu, G.; Zhu, J. Highly Monodispersed Fe_2WO_6 Micro-Octahedrons with Hierarchical Porous Structure and Oxygen Vacancies for Lithium Storage. *Chem. Engin. J.* **2021**, *413*, 127504.

21. Espinosa-Angeles, J.C.; Goubard-Bretesché, N.; Quarez, E.; Payen, C.; Sougrati, M.T.; Crosnier, O.; Brousse, T. Investigating the Cycling Stability of Fe_2WO_6 Pseudocapacitive Electrode Materials. *Nanomaterials* **2021**, *11*, 1405.

22. Panja, S.N.; Kumar, J.; Harnagea, L.; Nigam, A.K.; Nair, S. γ-Fe_2WO_6 – A Magnetodielectric with Disordered Magnetic and Electronic Ground States. *J. Magn. Magn. Mater.* **2018**, *466*, 354-358.

23. Schuler, R.; Norby, T.; Fjellvåg, H.; Defects and Polaronic Electron Transport in Fe_2WO_6. *Phys. Chem. Chem. Phys.* **2020**, *27*, 15541-15548.

24. Schuler, R.; Bianchini, F.; Norby, T.; Fjellvåg, H. Near-Broken-Gap Alignment between $FeWO_4$ and Fe_2WO_6 for Ohmic Direct p−n Junction Thermoelectrics. *ACS Appl. Mater. Interfaces* **2021**, *13*, 7416-7422.

25. Hassanpour, M.; Hosseini Tafreshi, S.A.; Amiri, O.; Hamadanian, M.; Salavati-Niasari, M. Toxic Effects of Fe_2WO_6 Nanoparticles towards Microalga Dunaliella salina: Sonochemical

Synthesis Nanoparticles and Investigate its Impact on the Growth. *Chemosphere* **2020**, *258*, 127348.

26. Nandiyanto, A.B.D.; Okuyama, K. Progress in Developing Spray-drying Methods for the Production of Controlled Morphology Particles. *Adv. Powder Technol.* **2011**, *22*, 1-19.

27. Stunda-Zujeva, A.; Irbe, Z.; Berzina-Cimdina, L. Controlling the Morphology of Ceramic and Composite Powders Obtained via Spray Drying – A review. *Ceram. Int.* **2017**, *43*, 11543-11551.

28. Rouquerol, J.; Llewellyn, P.; Rouquerol, F. Is the BET Equation Applicable to Microporous Adsorbents? *Studies Surf. Sci. Catal.* **2007**, *160*, 49-56.

29. Fauth, F.; Boer, R.; Gil-Ortiz, F.; Popescu, C.; Vallcorba, O.; Peral, I.; Fullà, D.; Benach, J.; Juanhuix, J. The Crystallography Stations at the Alba Synchrotron. *Eur. Phys. J. Plus* **2015**, *130*, 160.

30. Chapon, L.C.; Manuel, P.; Radaelli, P.G.; Benson, C.; Perrott, L.; Ansell, S.; Rhodes, N.J.; Raspino, D.; Duxbury, D.; Spill, E. et al, Wish: The New Powder and Single Crystal Magnetic Diffractometer on the Second Target Station. *Neutron News* **2011**, *22*, 22–25.

31. Rodríguez-Carvajal, J. Recent Advances in Magnetic Structure Determination by Neutron Powder Diffraction. *Phys. B Condens. Matter* **1993**, *192*, 55-69.

32. Zupan, K.; Marinsek, M.; Pejovnik, S.; Macek, J.; Zore, K. Combustion Synthesis and the Influence of Precursor Packing on the Sintering Properties of LCC Nanopowders. *J. Eur. Ceram. Soc.* **2004**, *24*, 1935-1939.

33. Waburg, M.; Müller-Buschbaum, H. $ZnTa_2O_6$, Ein Neuer Vertreter des tri-α-PbO_2-Typs (mit Ergänzenden Daten über $ZnNb_2O_6$). *Z. Anorg. Allg. Chem.* **1984**, *508*, 55-60.

34. Bernier, J.C.; Poix, P. Structural Study of Two Trirutile Oxide Containing Vanadium. Ann. Chim. (Paris), 1968, 14, 119.

35. Caubergh, S.; Matsubara, N.; Damay, F.; Maignan, A.; Fauth, F.; Manuel, P.; Khalyavin, D.D.; Vertruyen, B.; Martin, C. Original Network of Zigzag Chains in the β Polymorph of Fe_2WO_6: Crystal Structure and Magnetic Ordering. *Inorg. Chem.* **2020**, *59*, 9798-9806.

36. Thomas, G. ; Ropital, F. Influence des Gaz sur la Synthèse du Tungstate de Fer Fe_2WO_6 – 1. Etude Expérimentale. *Mater. Chem. Phys.* **1984**, *11*, 549-562.

37. Leiva, H.; Kershaw, R.; Dwight, K.; Wold, A. Preparation and Properties of the Systems $Fe_{2-x}Cr_xWO_6$, $Fe_{2-x}Rh_xWO_6$, and $Cr_{2-x}Rh_xWO_6$. *J. Solid State Chem.* **1983**, *47*, 293-300.

38. Müller, U. *Symmetry Relationships between Crystal Structures;* Oxford University Press: Oxford, 2013, p. 199.

39. Sherman, D.M.; Waite, T.D. Electronic Spectra of Fe^{3+} Oxides and Oxide Hydroxides in the Near IR to Near UV. *Am. Mineral.* **1985**, *70*, 1262-1269.

40. Morris, R.V.; Lauer, H.V.; Lawson, C.A.; Gibson, E.K.; Nace, G.A.; Stewart, C. Spectral and Other Physicochemical Properties of Submicron Powders of Hematite (α-Fe_2O_3), Maghemite (γ-Fe_2O_3), Magnetite (Fe_3O_4), Goethite (α-FeOOH), and Lepidocrocite (γ-FeOOH). *J. Geophys. Res.* **1985**, *90*, 3126-3144.

41. Marusak, L.A.; Messier, R.; White, W.B. Optical Absorption Spectrum of Hematite, αFe_2O_3 near IR to UV. *J. Phys. Chem. Solids* **1980**, *41*, 981-984.

42. Galuza, A.I.; Beznosov, A.B.; Eremenko, V.V Optical Absorption Edge in α–Fe_2O_3: The Exciton–Magnon Structure. *Low Temp. Phys.* **1998**, *24*, 726-729.

43. Chernyshova, I. V.; Ponnurangam, S.; Somasundaran, P. On the Origin of an Unusual Dependence of (Bio)chemical Reactivity of Ferric Hydroxides on Nanoparticle Size. *Phys. Chem. Chem. Phys.* **2010**, *12*, 14045-14056.

44. Dondi, M.; Matteucci, F.; Cruciani, G.; Gasparotto, G.; Tobaldi, D.M. Pseudobrookite Ceramic Pigments: Crystal Structural, Optical and Technological Properties. *Solid State Sci.* **2007**, *9*, 362-369.

45. Grave, D.A.; Yatom, N.; Ellis, D.S.; Toroker, M.C.; Rothschild, A. The “Rust” Challenge: On the Correlations between Electronic Structure, Excited State Dynamics, and Photoelectrochemical Performance of Hematite Photoanodes for Solar Water Splitting. *Adv. Mater.* **2018**, *30*, 1706577.

46. Liao, P.; Carter, E. A. Optical Excitations in Hematite (α-Fe_2O_3) via Embedded Cluster Models: A CASPT2 Study. *J. Phys. Chem. C* **2011**, *115*, 20795-20805.

47. Piccinin, S. The Band Structure and Optical Absorption of Hematite (α-Fe_2O_3): a First-Principles GW-BSE Study. *Phys. Chem. Chem. Phys.* **2019**, *21*, 2957-2967.

48. Meng, Y.; Liu, X.W.; Huo, C.F.; Guo, W.P.; Cao, D.B.; Peng, Q.; Dearden, A.; Gonze, X.; Yang, Y.; Wang, J. et al, When Density Functional Approximations Meet Iron Oxides. *J. Chem. Theory Comput.* **2016**, *12*, 5132-5144.

49. Liao, P.; Carter, E. A. Testing Variations of the GW Approximation on Strongly Correlated Transition Metal Oxides: Hematite (α-Fe_2O_3) as a Benchmark. *Phys. Chem. Chem. Phys.* **2011**, *13*, 15189-15199.

50. Snir, N.; Toroker, M.C.; The Operando Optical Spectrum of Hematite during Water Splitting through a *GW*–BSE Calculation. *J. Chem. Theory Comput.* **2020**, *16*, 4857-4864.

51. Gesesse, G.D.; Gomis-Berenguer, A.; Barthe, M.F.; Ania, C.O. On the Analysis of Diffuse Reflectance Measurements to Estimate the Optical Properties of Amorphous Porous Carbons and Semiconductor/Carbon Catalysts. *J. Photochem. Photobiol. A* **2020**, *398*, 112622.

52. Tauc, J.; Grigorovici, R.; Vancu, A. Optical Properties and Electronic Structure of Amorphous Germanium. *Phys. Stat. Sol.* **1966**, *15*, 627-637.

53. Botella, P.; Lopez-Moreno, S.; Errandonea, D.; Manjon, F.J.; Sans, J.A.; Vie, D.; Vomiero, A. High-Pressure Characterization of Multifunctional $CrVO_4$ *J. Phys.: Condens. Matter* **2020**, *32*, 385403.

54. Rajeshwar, K.; Hossain, M.K.; Macaluso R.T.; Janaky, C.; Varga, A.; Kulesza, P.J. Review—Copper Oxide-Based Ternary and Quaternary Oxides: Where Solid-State Chemistry Meets Photoelectrochemistry *J. Electrochem. Soc.* **2018**, *165*, H3192-H3206.

55. Roy, D.; Samu, G.F.; Hossain, M.K.; Janáky, C.; Rajeshwar K. On the Measured Optical Bandgap Values of Inorganic Oxide Semiconductors for Solar Fuels Generation, *Catal. Today* **2018**, *300*, 136–144.

56. Botella, P.; Errandonea D.; Garg, A.B.; Rodriguez-Hernandez, P.; Muñoz, A.; Achary, S.N.; Vomiero, A. High-Pressure Characterization of the Optical and Electronic Properties of $InVO_4$, $InNbO_4$, and $InTaO_4$ *SN Applied Sciences* **2019**, *1*, 389.

TOC Graphic

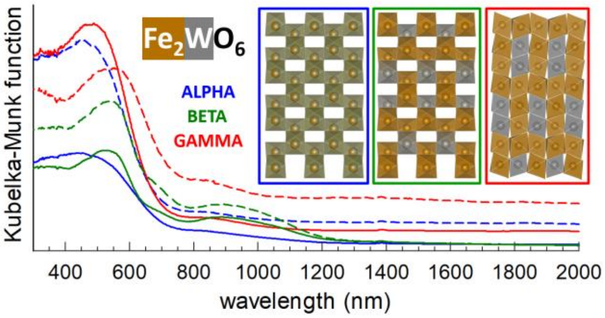

Fe_2WO_6
ALPHA
BETA
GAMMA
Kubelka-Munk function
400
600
800
1000
1200
1400
1600
1800
2000
wavelength (nm)